

# Investigation of the Microstructure and Rheology of Iridium Oxide Catalyst Inks for Low-Temperature Polymer Electrolyte Membrane Water Electrolyzers

Sunilkumar Khandavalli,<sup>†</sup> Jae Hyung Park,<sup>‡</sup> Nancy N. Kariuki,<sup>‡</sup> Sarah F. Zaccarine,<sup>§</sup> Svitlana Pylypenko,<sup>§</sup> Deborah J. Myers,<sup>‡</sup> Michael Ulsh,<sup>†</sup> and Scott A. Mauger<sup>\*,†,§</sup>

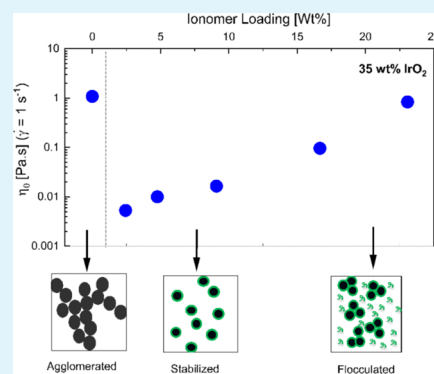
<sup>†</sup>Chemistry and Nanoscience Center, National Renewable Energy Laboratory, Golden, Colorado 80401, United States

<sup>‡</sup>Chemical Sciences and Engineering Division, Argonne National Laboratory, Lemont, Illinois 60439, United States

<sup>§</sup>Department of Chemistry, Colorado School of Mines, Golden, Colorado 80401, United States

**ABSTRACT:** We present an investigation of the structure and rheological behavior of catalyst inks for low-temperature polymer electrolyte membrane water electrolyzers. The ink consists of iridium oxide (IrO<sub>2</sub>) catalyst particles and a Nafion ionomer dispersed in a mixture of 1-propanol and water. The effects of ionomer concentration and catalyst concentration on the microstructure of the catalyst ink were studied. Studies on dilute inks (0.1 wt % IrO<sub>2</sub>) using zeta potential and dynamic light scattering measurements indicated a strong adsorption of the ionomer onto the catalyst particles which resulted in an increase in the  $\zeta$ -potential and the z-average diameter. Steady-shear and dynamic-oscillatory-shear rheological measurements of concentrated IrO<sub>2</sub> dispersions (35 wt % IrO<sub>2</sub>) indicated that the particles are strongly agglomerated in the absence of the ionomer. The addition of even a small amount of the ionomer (2.4 wt % with respect to total solids) caused the rheology to transition from shear thinning to Newtonian because of the reduction in agglomerated structure due to stabilization of the aggregates by the ionomer, consistent with the behavior of dilute inks. At intermediate ionomer loadings, between 2.4 and 9 wt %, the viscosity increased with increasing ionomer wt %, though remained Newtonian, predominantly due to the increasing ionomer volume fraction in the ink. For ionomer loadings greater than 9 wt %, the particles were found to be flocculated, likely induced by a dispersed ionomer. The flocculated inks exhibited strong shear-thinning and gel-like behaviors in steady-shear and oscillatory-shear rheology. The onset of flocculation was found to be sensitive to the catalyst concentration, where below 35 wt % of IrO<sub>2</sub>, flocculation was not observed. The rheological observations were further verified by ultra-small-angle X-ray scattering.

**KEYWORDS:** low-temperature polymer electrolyte membrane exchange water electrolysis, rheology, catalyst inks, iridium oxide, ionomer, catalyst layer



## INTRODUCTION

Hydrogen (H<sub>2</sub>) is an energy carrier used for several applications such as transportation and grid-scale energy storage and distribution (as supported by the US Department of Energy's H<sub>2</sub>@Scale initiative).<sup>1–3</sup> Currently, H<sub>2</sub> is primarily used for petroleum refining and ammonia production and is generated by steam methane reforming. Coupled with carbon-free energy, polymer electrolyte membrane water electrolyzers (PEMWEs) provide a pathway for carbon-free hydrogen generation for both transportation and industrial uses. In a PEMWE, water is electrochemically split into hydrogen at the cathode and oxygen at the anode.<sup>4</sup> Electrode kinetics of the catalyst layer (CL) are one of the limiting factors in PEMWE performance. Importantly, the microstructure of the CL strongly influences mass transport and other properties and thus plays a key role in the performance.<sup>4</sup> The CL microstructure is formed by the catalyst particles and an ionomer, which acts both as a binder for catalyst particles and as a proton-conducting medium. Typical catalysts in PEMWE

are an unsupported iridium oxide (IrO<sub>2</sub>)-based catalyst at the anode and noble metals such as Pt/Pd-based catalysts at the cathode.<sup>2</sup>

The CLs are fabricated through solution processing of a catalyst-containing ink, which is prepared by dispersing the catalyst and ionomer in a water–alcohol mixture.<sup>5</sup> The ink is coated onto a substrate (membrane, decal, or porous transport layer) by different methods such as spray-coating, blade-coating, rod-coating, or brush-painting. It is then dried to form the CL.<sup>2,4</sup> Several studies of CL microstructure–performance relationships suggest that the CL microstructure characteristics, such as the extent of the catalyst–ionomer interaction, continuity of the ionomer phase, and pore size distribution are critical for performance.<sup>4</sup> The final CL microstructure is influenced by the catalyst ink microstructure, which is dictated

**Received:** August 12, 2019

**Accepted:** November 7, 2019

**Published:** November 7, 2019



by the catalyst–ionomer–dispersion medium interactions, and how the coating and drying processes impact the structure.<sup>5–7</sup>

The ionomer content in the catalyst ink plays an important role in the CL electrochemical performance by facilitating proton transport as well as acting as a binder to maintain the CL structure. For optimal performance, the ionomer content must be sufficient to form a contiguous network for efficient proton conductivity but not so high that it significantly diminishes CL porosity, hindering gas/H<sub>2</sub>O transport, or electrically isolates the catalyst particles.<sup>8–10</sup> To date, the optimal ionomer fraction in the ink has been determined empirically, without a foundational understanding of how the interparticle interactions influence the optimal ionomer fraction for a given catalyst/ionomer system. Understanding of the ionomer–particle interactions and the impact of the bulk microstructure of the ink is critical to develop a framework to relate catalyst ink formulation to the CL microstructure and ultimately performance.<sup>11</sup>

Several fundamental colloidal science studies exist on the interactions between particles and charged polymers (ionomers and polyelectrolytes) and their impact on bulk dispersion microstructure.<sup>11,12</sup> Depending on the nature of these interactions, the polymer can either stabilize or flocculate the particles and have a marked impact on the bulk structure and the rheological properties of colloidal dispersions. However, we are unable to find any literature studies on PEMWE catalyst inks elucidating the interactions between the catalyst and ionomer and the impact on the ink microstructure.

Rheology is a sensitive technique to characterize the bulk microstructure of a broad range of materials.<sup>11,13</sup> Additionally, rheological properties are a strong predictor of their processing behavior in the manufacturing of the CL.<sup>14</sup> The rheological properties have been found to affect the coating characteristics such as, uniformity, thickness, and ink penetration into a porous substrate<sup>15–18</sup> and also the CL morphology in the drying process.<sup>19,20</sup> Thus, characterization of the rheological properties is critical toward establishing materials-processing-performance relationships.

In this paper, a study on PEMWE catalyst inks examining the nature of catalyst–ionomer interactions and their impact on the ink microstructure is presented. We investigate these interactions by studying the ink microstructure as a function of both the ionomer concentration and the catalyst concentration. We first study dilute catalyst inks using a combination of zeta potential ( $\zeta$ -potential) and dynamic light scattering (DLS). Next, we investigate the microstructure of concentrated ink dispersions through steady-shear and dynamic-oscillatory-shear rheology measurements. We then verify the rheological observations of the ink structure using ultra-small-angle X-ray scattering (USAXS).

## ■ EXPERIMENTAL SECTION

**Materials and Sample Preparation.** Iridium(IV) oxide (IrO<sub>2</sub>) catalyst powder (99.9% purity, 85% Ir min) was acquired from Alfa Aesar. The Brunauer–Emmett–Teller (BET) specific surface area and the pore volume were measured to be approximately 15–20 m<sup>2</sup>/g and 0.092 cm<sup>3</sup>/g, respectively. For both rheometry and USAXS measurements, the inks were prepared by adding the desired amount of IrO<sub>2</sub> (5–45 wt %) to a 1-propanol (Alfa Aesar) and water (Milli-Q) mixture and then adding the desired amount of Nafion (D2020, 1000 EW, Ion Power). The 1-propanol/H<sub>2</sub>O mass ratio was fixed at 1:1. The inks were dispersed using probe sonication for 2 min, followed by sonication for an additional 1 h in an ice water bath. The

DLS and  $\zeta$ -potential experiments were conducted on dilute IrO<sub>2</sub> inks, 0.1 wt %, to prevent multiple scattering in the measurements.

**N<sub>2</sub> Adsorption Experiments.** A Micromeritics ASAP 2020 was used to measure the N<sub>2</sub> adsorption isotherms. To eliminate any surface water, all the samples were degassed at 200 °C in vacuum before making the measurements. The BET surface area was determined in the general range of 0.01–0.15  $P/P_0$  (where  $P_0$  is the measured saturation pressure of N<sub>2</sub>). A single point desorption total pore volume of pores at  $P/P_0$  of 0.98 was used to determine the total pore volume. Using the Barrett–Joyner–Halenda model, the mesopore surface area and pore volumes were determined from the desorption data. To calculate the micropore volumes and surface areas, the mesopore values were subtracted from the total values.

**$\zeta$ -Potential and DLS.** A Zetasizer Nano ZS (Malvern Instruments Ltd, Malvern, UK) was used to conduct  $\zeta$ -potential and DLS measurements. A high-concentration zeta cell (ZEN1010) that allows tests on more concentrated solutions was used.<sup>21</sup> All the tests were done at 25 °C. A Helmholtz–Smoluchowski equation<sup>22</sup> was used to calculate zeta potential where the particle size was assumed to be larger than the electric double layer thickness, which is valid here. At least five readings were taken to ensure repeatability of the measurements. A pH meter (Thermo Fisher Scientific, Orion 4-Star) was used to measure the pH of the inks. To adjust the pH value of the inks, 0.01 M H<sub>2</sub>SO<sub>4</sub> was used.

**Transmission Electron Microscopy.** Transmission electron microscopy (TEM) images were collected by pipetting one drop of the catalyst ink onto the carbon film 300 mesh Cu grids and imaged using an FEI Talos F200x operated at 200 kV.

**X-ray Scattering.** The aggregated structure of the IrO<sub>2</sub> ink was characterized using X-ray scattering at beam line 9ID-C at the Advanced Photon Source (APS) at Argonne National Laboratory. The inks, which were prepared as described earlier, were filled into a glass capillary tube (1 mm diameter) and then sealed by an epoxy resin. In order to prevent any air bubbles, the capillary tubes were filled completely with the inks. The samples were placed in the beamline hutch, horizontally, and a monochromatic X-ray beam in the range of 16.8–21 keV was exposed. A combination of USAXS–SAXS by a Bonse–Hart camera for USAXS and a Pilatus 100 K detector for pinhole SAXS was used to measure the scattered X-ray intensity. The scattering vector,  $q$ , of the measurement ranges between  $10^{-4}$  and  $6 \times 10^{-2}$  Å<sup>-1</sup> for the USAXS and  $3 \times 10^{-2}$  and 1 Å<sup>-1</sup> for the pinhole SAXS.

Unlike other X-ray techniques, the ionomer in the catalyst ink is not damaged by the USAXS measurement. The X-ray beam in the USAXS instrument is unfocused and is relatively large (0.8 mm × 0.8 mm), and the flux density in the USAXS instrument is much lower than that in standard synchrotron SAXS instruments with focusing even with relatively high total photon flux. The scattering vector is inverse of the object size, given as,  $q = 4\pi \sin(\theta/2)/\lambda$ , where  $\lambda$  is the wavelength of the X-ray beam. Based on the  $q$  range, the measurement length scale spans approximately between 1 nm and 1  $\mu$ m. The background scattering data of the dispersion medium (50 wt % 1-propanol and 50 wt % water) were also collected. This was subtracted from the scattering data for each catalyst ink. The data analysis was performed on a modeling macro package Irena (APS, X-ray science division, beamline 9ID-C) and Igor Pro (WaveMetrics, OR) platform.

**Rheology Measurement Protocol.** A stress-controlled rheometer (Bohlin Gemini HR Nano, Malvern Instruments) was used to perform rheology measurements. A stainless-steel parallel plate geometry (40 mm diameter) at 250  $\mu$ m gap was used for measurements. All the tests were conducted at 25 °C. A solvent saturation trap was used in order to minimize any solvent evaporation during measurements. To erase any sample loading history on the measurements, preconditioning of the samples was performed by preshearing at 1000 s<sup>-1</sup> for 30 s, followed by a resting step for 10 s. In the steady shear rheology measurements, the stress was varied logarithmically in decreasing direction in the range of 40–0.0001 Pa.

For dynamic-oscillatory-shear measurements, the same preshear protocol was followed as that for steady shear. For amplitude-sweep measurements, the frequency was fixed at 0.5 Hz and the stress was

increased logarithmically from 0.0001 to 200 Pa. For frequency-sweep tests, the strain was fixed within the linear viscoelastic regime and the frequency was varied logarithmically from 5 to 0.05 Hz.

## RESULTS AND DISCUSSION

The following sections present a discussion of the characterization of IrO<sub>2</sub> catalyst inks. First, we studied the nature of the ionomer interaction with the catalyst particles using a combination of  $\zeta$ -potential and DLS measurements on dilute inks. The interaction between catalyst aggregates and the ionomer was examined by varying the ionomer concentration for a fixed IrO<sub>2</sub> concentration. Next, we used rheometry to investigate the impact of catalyst–ionomer interactions on the bulk microstructure in more concentrated inks. Finally, we discuss the possible implications of our findings on optimizing the catalyst ink formulations and processing for the fabrication of the CL.

**$\zeta$ -Potential and DLS.** The  $\zeta$ -potential measurements performed on the dilute IrO<sub>2</sub> dispersions (0.1 wt %) at different ionomer loadings are shown in Figure 1. The ionomer

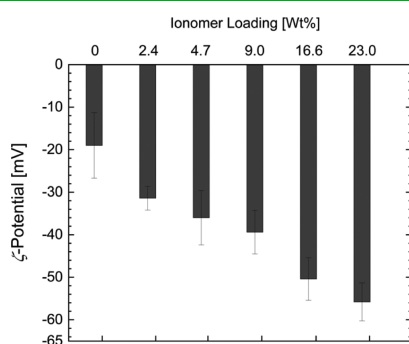


**Figure 1.** Zeta potential of 0.1 wt % IrO<sub>2</sub> dispersions for different ionomer loadings.

loading is the mass fraction of the ionomer with respect to total solids mass, given as  $\frac{m_{\text{ionomer}}}{m_{\text{ionomer}} + m_{\text{IrO}_2}} \times 100\%$ . The  $\zeta$ -potential of bare particles (0 wt % ionomer) indicates that the particles are negatively charged. The  $\zeta$ -potential becomes more negative with increasing ionomer loading. Nafion is an anionic ionomer consisting of sulfonic acid (SO<sub>3</sub><sup>−</sup>H<sup>+</sup>) functional groups on the side-chain segments. The negative increase in  $\zeta$ -potential on the ionomer addition indicates the adsorption of the ionomer onto the particle surface.<sup>23–25</sup> As both the particles and the sulfonic groups of the ionomer are similar in charge (negative), electrostatic repulsion would exist and oppose ionomer adsorption. However, previous studies have observed the adsorption of anionic polymers to negatively charged particles, and the adsorption mechanisms has been attributed to nonelectrostatic interactions such as hydrogen-bonding or hydrophobic interactions.<sup>26</sup> Similar interactions could be driving the ionomer adsorption via the hydrophobic perfluorinated backbone or hydrogen-bonding between ether-oxygen or sulfonic groups of the ionomer segments and the surface hydroxyl groups of the particles, where the latter mechanism is more likely as the particles are relatively hydrophilic.<sup>27</sup>

The influence of ionomer addition on the IrO<sub>2</sub> agglomerate size in the inks was examined by DLS as shown in Figure 2. The measured  $Z_{\text{avg}}$  diameter as a function of the ionomer content is shown in Figure 2a. With the addition of the

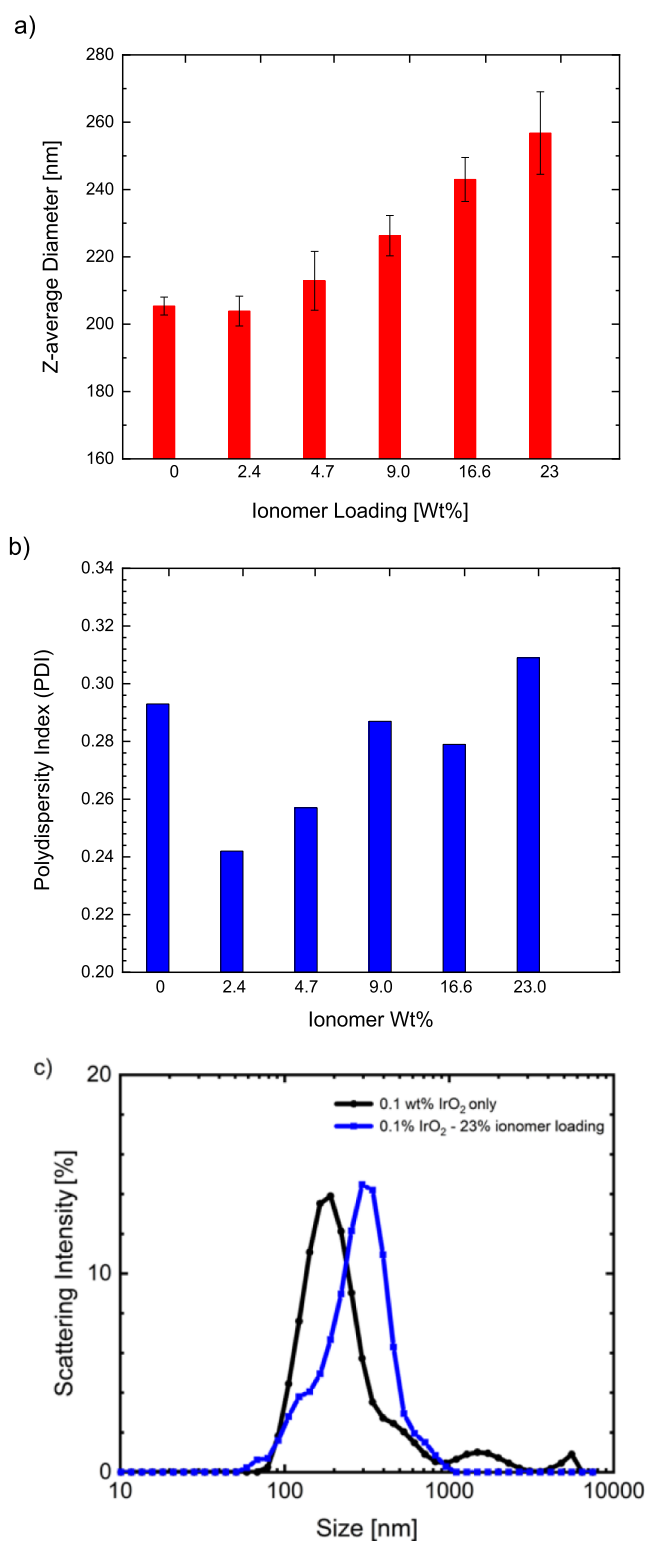


**Figure 2.** (a) Z-average diameter and (b) polydispersity index of 0.1 wt % IrO<sub>2</sub> dispersions for different ionomer loadings. (c) Scattering intensity vs diameter distribution plots for 0.1 wt % IrO<sub>2</sub> dispersions both without and with the ionomer (23 wt %).

ionomer up to 4.7 wt %, the  $Z_{\text{avg}}$  does not change significantly. It is likely there is limited agglomeration because the IrO<sub>2</sub> concentration was very dilute (particle volume percent,  $\Phi \approx 7 \times 10^{-3}\%$ ), making the agglomeration kinetics slow.<sup>28</sup> However, a slight decrease in the polydispersity of the dispersions can be

observed in Figure 2b which can be attributed to some increased stability in the dispersions. For ionomer concentrations larger than 4.7 wt %, the  $Z_{\text{avg}}$  increases by  $\sim 50$  nm at a 23 wt % ionomer loading. This can be attributed to a combination of both the adsorbed ionomer thickness and the Debye length (counter-ion cloud surrounding the charged surface) which increase the effective hydrodynamic size of the particles.<sup>28</sup> The Debye length ( $\kappa^{-1}$ ) can be estimated using the equation<sup>29</sup>

$$\kappa^{-1} = \sqrt{\left( \frac{\epsilon_0 \epsilon_r kT}{2z^2 e^2 I} \right)} \quad (1)$$

Here  $\epsilon_r$  and  $\epsilon_0$  are relative permittivity of dispersion medium (42.5<sup>30</sup>) and absolute permittivity of vacuum ( $8.85 \times 10^{-12}$  F/m), respectively,  $I$  is the ionic strength ( $I = [\text{H}^+] \approx 10^{-4}$  M of the ink was assumed, as the ink is salt-free), and  $z$  is the ion valency. For the ink studied,  $\kappa^{-1} \approx 20$  nm. Prior studies on the structure of ionomer solutions show a rod-like agglomerated structure of the ionomer with radius 1–2 nm and 10 s of nm in length using techniques such as SAXS and cryo-TEM.<sup>31,32</sup> Accounting for the Debye length contribution to the  $Z_{\text{avg}}$  of the particles, the increase due to adsorbed ionomer thickness is  $\sim 25$  nm at 23 wt % ionomer loading which suggests the adsorption of several ionomer agglomerates onto the  $\text{IrO}_2$  surface.

The adsorption of the ionomer onto particles has been previously shown to stabilize dispersed particles such as carbon black, platinum on carbon black (Vulcan), and  $\text{IrO}_2$  (dispersed in ethanol) against van der Waals agglomeration.<sup>11,24,25,33</sup> As the stabilization effect of the ionomer on  $\text{IrO}_2$  agglomerates is not very evident from  $Z_{\text{avg}}$ , we have additionally evaluated ink stability by visually inspecting the settling behavior of more concentrated inks (1 wt %  $\text{IrO}_2$ ). As shown in Figure 3, inks

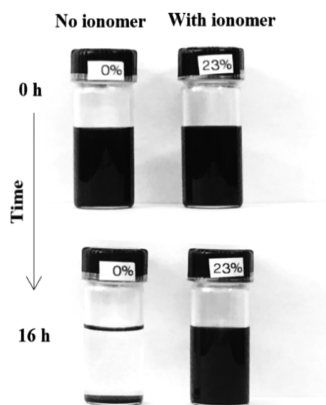


**Figure 3.** Visual inspection of the settling behavior of 1 wt %  $\text{IrO}_2$  ink samples over 16 h duration. Inks without and with the ionomer (23 wt %) are compared.

without the ionomer settle almost completely in 16 h, but inks with the ionomer (23 wt % ionomer loading) remain suspended. These observations provide much clearer evidence of agglomerate stabilization by the ionomer. We expect a similar outcome for 0.1 wt %  $\text{IrO}_2$  inks but with longer settling times compared to 1%  $\text{IrO}_2$  inks due to slower agglomeration kinetics at dilute concentrations.<sup>28,34</sup>

The adsorbed ionomer can stabilize particles through a combination of steric and electrostatic mechanisms called the “electrosteric stabilization” mechanism.<sup>12,35</sup> The electrostatic

repulsion, which is long-ranged, is provided by the charged groups of the polymer, which are sulfonic acid groups in the case of Nafion. It is well-described by Derjaguin–Landau–Verwey–Overbeek theory,<sup>36,37</sup> which describes the electrostatic stability of aqueous colloidal dispersions.<sup>20,33</sup> Steric repulsion is imparted by the physical repulsion from the adsorbed polymer segments on the particle surface when the particles approach contact distances. This stabilization against agglomeration is an important factor for optimizing electrode performance. In fuel cells, poor dispersion of both catalyst particles and the ionomer in the CLs has been shown to limit reactant gas transport and cause flooding, resulting in significant mass transport losses affecting performance.<sup>38</sup>

In the ionomer concentration effect study here, the  $\zeta$ -potential and  $Z_{\text{avg}}$  measurement values may not have been solely due to the adsorbed ionomer but could also be influenced by the changes in dispersion medium properties such as pH and ionic strength, which were not kept constant. On increasing ionomer loading from 0 to 23 wt %, the pH of the medium decreased from 6 to 3.8 due to the increased concentration of dissociated protons from the sulfonic groups, which also consequently increased the ionic strength of the dispersion medium. Both pH and ionic strength strongly influence electrostatic interactions by affecting the double layer charge environment of the particles (surface charge and double layer thickness) and thus particle agglomeration.<sup>28,39</sup> Therefore, the effect of pH on the  $\zeta$ -potential and  $Z_{\text{avg}}$  of pure  $\text{IrO}_2$  inks was also studied. As shown in Figure 4a, with decreasing medium pH, the  $\zeta$ -potential shifted closer to zero, and

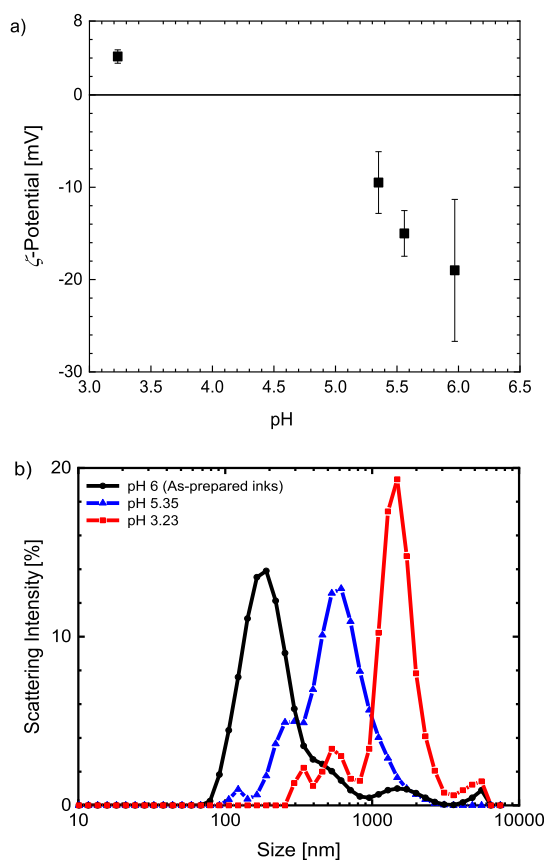


**Figure 4.** (a) Zeta potential and (b) size distribution by scattering intensity comparisons of 0.1 wt %  $\text{IrO}_2$  inks (no ionomer) at different adjusted solvent pH.



ultimately reversed the sign to become positive at the lowest pH. The size distribution plots in Figure 4b show an increase in particle agglomeration with a reduction in the pH. These trends in  $\zeta$ -potential and  $Z_{\text{avg}}$  as a function of pH follow the general trend observed in aqueous colloidal dispersions.<sup>28,39</sup> Decreasing the medium pH shifts the  $\zeta$ -potential toward the point of zero charge due to protonation of the particle surface, which results in particle agglomeration due to the decrease in the electrostatic repulsive potential of the particles. The pH effect on both the  $\zeta$ -potential and the agglomerated structure is opposite to the ionomer concentration effect on the measurements. These results confirm that the  $\zeta$ -potential and  $Z_{\text{avg}}$  observations on the inks with the ionomer are dominated by the ionomer–particle interactions rather than the pH changes.

The observations in this section confirm an attractive interaction between ionomer and catalyst particles, where both  $|\zeta|$ -potential and  $Z_{\text{avg}}$  increase due to adsorption of the ionomer onto the particles. The observations are limited to dilute ink concentrations where the agglomeration levels are low as necessitated by the DLS technique. In practice, catalyst inks can vary in concentration, ranging from dilute to concentrated (e.g. 0.04–22 wt %<sup>40,41</sup>) for processing through various coating methods. As the particle concentration is increased, the inter-particle and ionomer–particle interactions are expected to increase, affecting the bulk ink microstructure more significantly. In the next sections, we will investigate the ink structure at a wider range of  $\text{IrO}_2$  concentrations, from dilute to concentrated inks, using a combination of rheometry and USAXS techniques.

**Rheology. Particle Dispersions without the Ionomer.** We first studied the rheological behavior of pure particle dispersions without the ionomer. The particle concentration was varied from 5 to 45 wt %. The steady-shear rheological behavior at different particle concentrations is shown in Figure 5. The low-shear viscosity increases with increasing particle

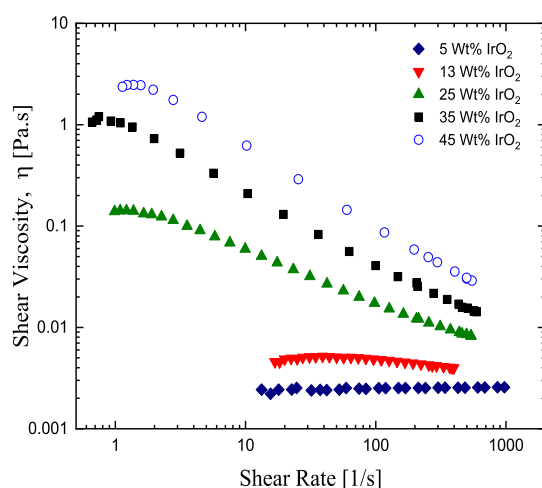


**Figure 5.** Steady-shear viscosity data of inks (no ionomer) for different  $\text{IrO}_2$  concentrations.

concentration due to a corresponding increase in the energy dissipation.<sup>28,34</sup> The rheological behavior is Newtonian until 13 wt %, beyond which the dispersions begin to exhibit shear thinning. The magnitude of shear thinning increases with increasing particle concentration. This shear thinning behavior is due to the breakdown of particle agglomerates and/or particle rearrangements induced by hydrodynamic shear

forces.<sup>42</sup> At these higher concentrations, we are able to better observe the agglomeration behavior of  $\text{IrO}_2$ , which we were not able to observe in the dilute inks used for DLS. In the Newtonian regime, where the microstructure is under equilibrium, Brownian forces are dominant and will quickly restore any deformation-induced changes in the structure to equilibrium.<sup>28</sup> For larger particle concentrations, the onset of shear-thinning behavior beyond a critical shear-rate is due to hydrodynamic forces becoming dominant over the Brownian forces and indicates an agglomerated ink microstructure. This effect of particle concentration on the rheological behavior is consistent with literature observations of other particle dispersions.<sup>11,43</sup>

To better understand the structure of the dispersions and the extent of deviation from well-dispersed colloidal dispersions, we compared the measured viscosity against theoretical/semi-empirical models for well-dispersed (hard-sphere and repulsive interparticle interactions) colloidal dispersions. Both the low-rate relative viscosity ( $\eta_{r,0}$ ) and high-rate relative viscosity ( $\eta_{r,\infty}$ ) are shown in Figure 6, where

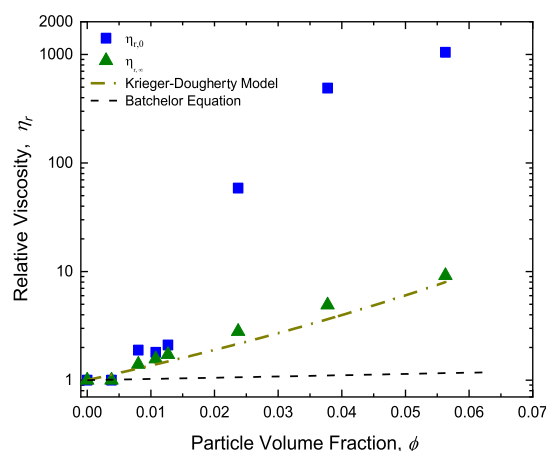


**Figure 6.** Low-shear-rate and high-shear-rate relative viscosity of inks (no ionomer) for different  $\text{IrO}_2$  particle volume fractions. Dashed line is a plot of the Batchelor equation,  $\eta_{r,\infty} = 1 + B\phi + B_1\phi^2$ , where the coefficients  $B$  and  $B_1$  were 2.5 and 6, respectively. Dot-dashed line is the high-shear-rate viscosity data fit to the Krieger–Dougherty model

$\eta_{r,\infty} = \left(1 - \frac{\phi}{\phi_{\text{max}}}\right)^{-[\eta]\phi_{\text{max}}}$ , where  $[\eta] = 30$  and  $\phi_{\text{max}} = 0.16$ , are intrinsic viscosity and maximum volume fraction, respectively, obtained from the best fit to the model.

$\eta_r$  is the relative viscosity  $\eta/\eta_m$  and  $\eta_m$  is the dispersion medium viscosity. The particle volume fraction ( $\phi$ ) was estimated based on the mass fractions assuming an  $\text{IrO}_2$  particle density of  $\rho_p = 11.66 \text{ g/cm}^3$  (as provided by the supplier) and dispersion media density of  $\rho_m = 0.925 \text{ g/cm}^3$  (50 wt % 1-propanol and 50 wt %  $\text{H}_2\text{O}$ ).<sup>30</sup> This estimation results in a  $\phi$ -range of 0.004–0.06, which includes both the dilute and semi-dilute concentration regimes. The viscosity prediction by Batchelor's theory<sup>44</sup> for semi-dilute hard-sphere particle dispersions is also shown in Figure 6 and is given by

$$\eta_{r,\infty} = 1 + B\phi + B_1\phi^2 \quad (2)$$

where  $B$  is Einstein's coefficient ( $B = 2.5$ ) and the coefficient  $B_1$  accounts for hydrodynamic interactions ( $B_1 = 6$  for limiting high-shear rates).<sup>45</sup> We observe that the experimental viscosities ( $\eta_{r,0}$  and  $\eta_{r,\infty}$ ) strongly deviate from the model.

This suggests that the particles are likely agglomerates that are not completely broken down at the high-shear rates experienced in this measurement. An agglomerated structure increases the effective volume fraction of the dispersions, leading to a departure from the semi-dilute regime where the Batchelor's theory is invalid.<sup>11</sup> Therefore, we examine the scaling behavior by fitting the high shear-rate viscosity data to the Kreiger–Dougherty model,<sup>46</sup> a commonly used semi-empirical model for a variety of dispersions, which is applicable in the concentrated regime, given as

$$\eta_{r,\infty} = \left[ 1 - \frac{\phi}{\phi_{\max}} \right]^{-[\eta]\phi_{\max}} \quad (3)$$

where  $[\eta]$  is the intrinsic viscosity and depends on the particle shape and interaction with the solvent and  $\phi_{\max}$  is the maximum particle volume fraction. As the inks at higher concentrations did not show a clear low-shear Newtonian plateau in our experiments, we have used the high-shear data to fit to the model. At high shear-rates, the contribution of the interparticle interactions to the viscosity would be minimal and  $\eta_{\infty}$  is predominantly influenced by hydrodynamic forces. The Kreiger–Dougherty model fit to the data is shown in Figure 6 and fits the measured data reasonably well. The  $[\eta]$  and  $\phi_{\max}$  obtained from the best fit to the data are 30 and 0.16, respectively. For spherical particles,  $[\eta]$  is 2.5, while for anisotropic shaped particles,  $[\eta]$  has been reported to be much greater, up to 80.<sup>47,48</sup> A larger  $[\eta]$  value of IrO<sub>2</sub> particles compared to spherical particles, by 12X, suggests a more anisotropic (or irregular) shape of the particles. Further, the  $\phi_{\max}$  of hard-sphere dispersions is 0.71 at limiting high shear-rates.<sup>49</sup> The much smaller value of  $\phi_{\max} \approx 0.16$  indicates an agglomerated structure of IrO<sub>2</sub> particles, a combination of both primary aggregates as well as agglomerates of primary aggregates that are not completely broken down by shear forces.<sup>47</sup> The comparison of the viscosity data with the Kreiger–Dougherty model indicates the strong agglomerated nature of the IrO<sub>2</sub> dispersions where the weak surface charge of the particles, as indicated by the low  $\zeta$ -potential, is not sufficient to stabilize against van der Waals agglomeration.

To confirm the results of the Kreiger–Dougherty model, the structure of dried IrO<sub>2</sub> inks was also visualized through TEM in Figure 7 to confirm the anisotropic and agglomerate structure of IrO<sub>2</sub> particles. While agglomerates ranging from tens of nanometers to tens of micrometers were observed

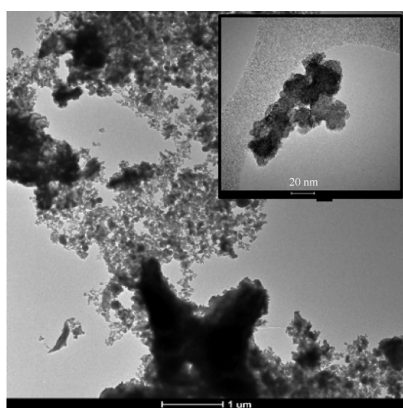


**Figure 7.** TEM images of a dried IrO<sub>2</sub> ink with no ionomer. The inset shows an isolated primary aggregate at a high magnification.

consistent with rheological observations, the drying process during the TEM sample preparation is also likely to influence the agglomerated structure. However, the images are at least qualitatively consistent with the rheological measurements. The inset image shows the anisotropic structure of a primary aggregate which also supports the large  $[\eta]$  obtained from the Kreiger–Dougherty model fit to the viscosity data.

**Particle Dispersions with the Ionomer.** *Effect of Ionomer Concentration.* Next, we examined the effect of ionomer loading on the ink microstructure and rheology for a concentrated IrO<sub>2</sub> ink. The ionomer loading was varied from 2.4 to 23 wt %. Here, the IrO<sub>2</sub> particle concentration was held at 35 wt %. The steady-shear rheological behavior at different ionomer loadings is shown in Figure 8. With the addition of a

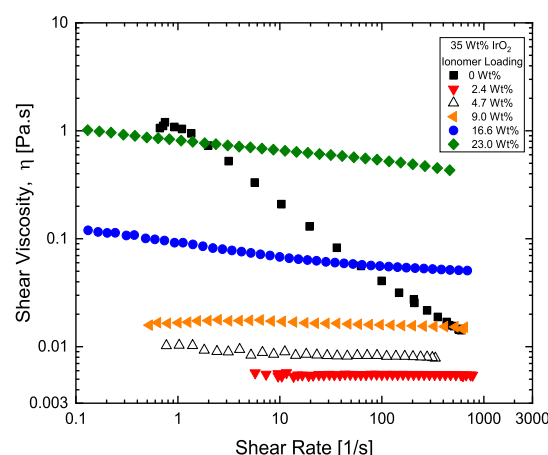


**Figure 8.** Steady-shear viscosity data of 35 wt % IrO<sub>2</sub> dispersions at different ionomer loadings.

small amount of the ionomer (2.4 wt %) to the particle dispersions, the low-shear viscosity drops significantly, by over 100X, and the steady-shear rheological behavior changes from shear-thinning to Newtonian. This suggests a strong reduction in the agglomerated structure of the dispersions.<sup>42</sup> Adsorption of the ionomer onto the particles was confirmed by an increase in the  $|\zeta|$ -potential and  $Z_{\text{avg}}$  values in dilute inks as discussed previously. Here, we were able to clearly observe the stabilization of IrO<sub>2</sub> agglomerates by the ionomer. The influence of the ionomer on the agglomerated structure is much more pronounced in the concentrated inks, where agglomerates are significant compared to the dilute inks used for DLS and  $\zeta$ -potential measurements. This transition from an agglomerated, shear-thinning ink to a stabilized, Newtonian ink with the addition of the ionomer is the same as what has been previously observed for carbon black dispersions.<sup>11,50</sup>

The catalyst ink stabilization by ionomer addition to the IrO<sub>2</sub> ink was further verified through USAXS/SAXS measurements. In Figure 9a, the scattered intensity ( $I(q)$ ) versus scattering vector ( $q$ ) for the dispersions without the ionomer and with 2.4 wt % ionomer is presented. Note that the IrO<sub>2</sub> concentrations in Figure 9 are 25 wt % and not 35 wt % as in Figure 8. We estimated the radius of gyration,  $R_g$ , of the aggregates/agglomerates from a unified fitting to the primary Guinier-knee for  $q$  below  $0.01 \text{ \AA}^{-1}$ .  $R_g$  for the dispersion with the ionomer is 54 nm, whereas  $R_g$  for the dispersion without the ionomer is 465 nm. We also compared the power-law scaling exponent of the intensity at low- $q$  ( $<0.001 \text{ \AA}^{-1}$ ),  $I(q) \approx q^{-d_f}$ , where  $d_f$  is the mass fractal dimension.  $d_f$  represents the

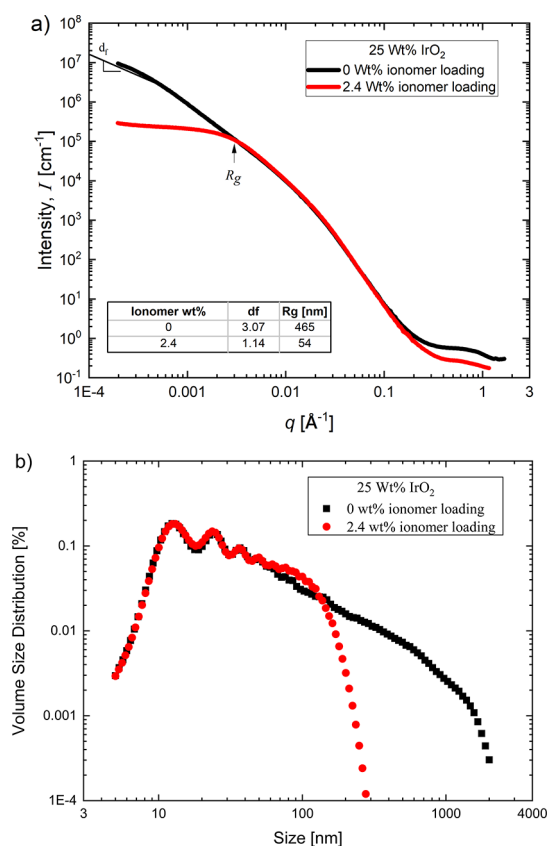


**Figure 9.** (a) USAXS scattering curves. Tabulated values of the mass fractal dimension  $d_f$  from  $I(q) \approx q^{-d_f}$  power-law fit to low- $q$  data and the radius of gyration  $R_g$  at a lower- $q$  region from Guinier fit to the data are also shown in pane (a) and (b) volume size distribution of the 25 wt %  $\text{IrO}_2$  dispersions without and with ionomer loadings (2.4 wt %).

agglomerated structure level (mass fractal), where a larger  $d_f$  indicates a greater level of agglomeration.<sup>51,52</sup> The low- $q$  intensity and the  $d_f$  values are lower with the ionomer ( $d_f \approx 1.14$ ) compared to without the ionomer ( $d_f \approx 3.07$ ). These data indicate less agglomerated dispersions with the ionomer compared to the dispersions without the ionomer. The corresponding volume size distribution is shown in Figure 9b. Without the ionomer, there is a sizeable population from 300 nm to over 1000 nm. With the addition of the ionomer, this population decreases substantially, with a majority of the population between 10 and 100 nm. These results corroborate the rheological analysis and indicate a reduction in  $\text{IrO}_2$  agglomerates with the addition of the ionomer, resulting from electrosteric stabilization of the particles.

With the additional ionomer beyond the initial 2.4 wt %, the low-shear viscosity begins to increase, as shown in Figure 8. It remains Newtonian up to 9 wt % and then begins to display some shear thinning, which is much weaker than was observed for the ionomer-free ink. The increase in the low-shear viscosity beyond 2.4 wt % ionomer suggests that the viscosity contribution from the added ionomer is likely dominating the behavior compared to any further stabilization of the agglomerates due to continued ionomer adsorption onto the particles. Alternatively, the ionomer could remain as excess/dispersed in the solvent when the adsorption onto particle surface reaches saturation. In either case, the ionomer contributes to the overall solid volume fraction and increase

the viscosity. The exact state of the ionomer in the ink as function of ionomer loading needs further investigation.

**Dynamic Oscillatory Shear Rheology.** The microstructure of particle dispersions is often viscoelastic, which can both store and dissipate energy. However, steady-shear rheology captures only the purely viscous nature of the microstructure. Characterizing the viscoelasticity of catalyst inks through dynamic oscillatory shear rheology could offer more insights into the ionomer–particle interactions and the bulk structure<sup>34</sup> and potentially the processing behavior of the ink during a CL coating process.<sup>16,53</sup> Thus, the characterization of viscoelastic properties is critical to understanding property–processing relationships. The viscoelastic properties, storage modulus  $G'$  and viscous modulus  $G''$ , which quantify elasticity and dissipation of the structure, respectively, were characterized both as a function of deformation frequency and deformation amplitude. The effects of ionomer loading and the catalyst concentration on the viscoelasticity of the inks will be presented.

The frequency-sweep and the amplitude-sweep measurements at different ionomer concentrations in the inks are presented in Figure 10a,b. Examining the scaling behavior for  $G'$  and  $G''$  with frequency ( $\omega$ ) at 0 wt % ionomer, we observe that both moduli scale similarly as a function of  $\omega$ , with  $G' \approx G'' \approx \omega^n$ , but the scaling exponent,  $n$ , varies between low and

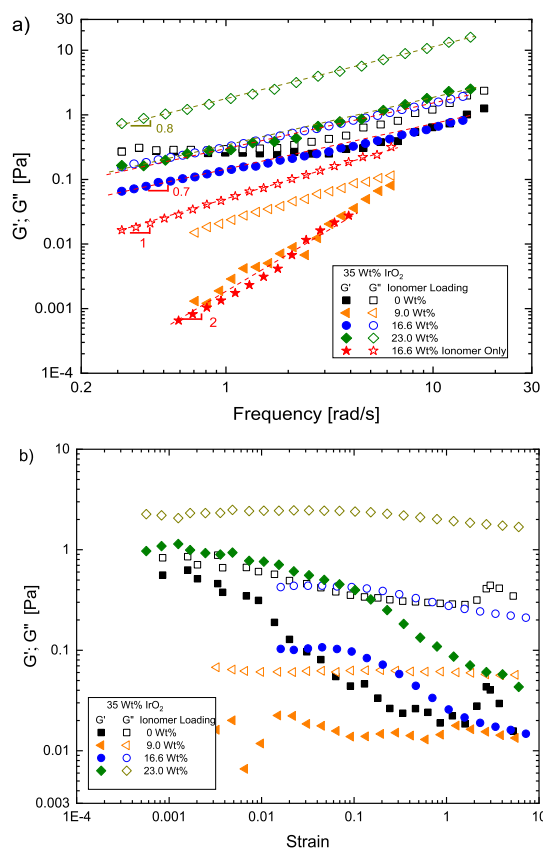


**Figure 10.** (a) Frequency-sweep measurements: elastic ( $G'$ ) and loss ( $G''$ ) moduli as a function of frequency, for 35 wt %  $\text{IrO}_2$  dispersions for different ionomer loadings. The data for 7 wt % pure ionomer dispersion (equivalent to 16.6 wt % loadings in ink) are also included. The lines are only a guide to the eye. (b) Amplitude-sweep measurements:  $G'$  and  $G''$  as a function of strain amplitude, for 35 wt %  $\text{IrO}_2$  dispersions for different ionomer loadings.



high frequency. For the low- $\omega$  region ( $\omega < 2$  rad/s), the moduli exhibit a frequency-independent plateau with  $G' \approx G''$ . This is indicative of a gel-like behavior where the applied  $\omega$  is faster than the longest relaxation time of the ink microstructure ( $\omega\tau_D \times D_s \gg 1$ ), and the structure is unable to relax completely by Brownian motion.<sup>28,34</sup>  $\tau_D$  is the relaxation time scale associated with Brownian diffusion of particles, given as  $\tau_D \sim r^2/D_s$ <sup>28</sup> where  $r$  and  $D_s$  are the particle radius and self-diffusion coefficient, respectively.  $\tau_D$  increases with increasing particle agglomeration due to both an increase in  $r$  and a decrease in  $D_s$ ,<sup>54</sup> causing the behavior to approach a gel. The gel-like response can be attributed to the agglomerated structure of the dispersions, as shown previously via steady-shear rheology and USAXS measurements. In the high- $\omega$  region ( $\omega > 2$  rad/s), the behavior changes from gel-like to more viscous-like, where  $G'' > G'$ . Here, the moduli become frequency-dependent, with a scaling of  $G' \approx G'' \approx \omega^1$ . This transition in the moduli response can be attributed predominantly to an increase in hydrodynamic forces at large  $\omega$ . The agglomerated structure of the inks without the ionomer is further evidenced by the amplitude-sweep behavior shown in Figure 10b. Both  $G'$  and  $G''$  decline with increasing strain amplitude (called strain-softening and strain-thinning, respectively) by  $\sim 3\times$  and  $\sim 30\times$ , respectively, due to break-down of the agglomerates by hydrodynamic forces. This is consistent with the agglomerate break-up observed at high-shear rates in the steady shear data.

At 9 wt % ionomer, the moduli scaling of frequency-sweep response changes to  $G' \approx \omega^1$  and  $G'' \approx \omega^2$ , where  $G'' > G'$ . Such scaling behavior is a characteristic response of liquid-like materials.<sup>34</sup> The viscous response ( $G''$ ) is Newtonian-like (dynamic viscosity  $\eta' = G''/\omega = \text{constant}$ ) and the elasticity is small, where  $G'$  declines much faster than the viscous modulus with a decreasing frequency. The transition from a gel-like to liquid-like response upon the addition of the ionomer is due to the reduction in the agglomerated structure of the dispersion by the ionomer stabilizing the IrO<sub>2</sub> particles, consistent with the steady-shear rheology results. The corresponding amplitude-sweep behavior in Figure 10b shows a strain-independent response of  $G'$  and  $G''$  as expected, which confirms that agglomeration is minimal.

With further increases in ionomer loadings beyond 9 wt % up to 23 wt %, the moduli magnitudes begin to increase and the behavior predominantly remains viscous-like with  $G'' > G'$  throughout the frequency range. However, the moduli scaling behavior changes, where they now scale similarly with frequency as  $G' \approx G'' \approx \omega^n$ , where  $n \approx 0.7$  and  $0.8$  for 16 and 23 wt % ionomer, respectively. It is unlikely this power-law behavior is arising from any dispersed/excess free ionomer that can potentially exist at large ionomer loadings in the ink. The frequency-sweep response of a pure ionomer dispersion at the same concentration as in the IrO<sub>2</sub> ink with 16.6 wt %, which is also shown in Figure 10a, is purely liquid-like ( $G' \approx \omega^1$  and  $G'' \approx \omega^2$ ). This suggests that the power-law response of the inks is associated with structure growth arising from attractive interactions between IrO<sub>2</sub> particles that are saturated by ionomer coverage. The power-law scaling with  $G' < G''$  and  $0 < n < 1$  is similar to the response of materials with a fractal or cluster-like structure approaching a percolated network structure (i.e. near the gel-point).<sup>55</sup> Such scaling behavior has been observed in flocculated colloidal dispersions where attractive interparticle interactions are at play.<sup>54,56</sup> Therefore, the power-law response at large ionomer loadings suggests the

existence of a fractal-like flocculated structure of the particles. The corresponding amplitude behavior at 16 and 23 wt % ionomer loadings in Figure 10b also indicates the presence of a flocculated microstructure. In both cases,  $G'$  and  $G''$  exhibit a weak strain-thinning behavior, consistent with the shear-thinning behavior seen in the steady-shear rheology data, and a strong strain-softening behavior ( $\sim 10\times$  greater than strain-thinning), respectively. These nonlinear viscoelastic responses can be associated with the breakdown of the flocculated microstructure by large shear deformations.<sup>57</sup>

To further verify the flocculated structure of inks, the ink structure was characterized by USAXS at different ionomer loadings, as shown in Figure 11. We observe an increase in

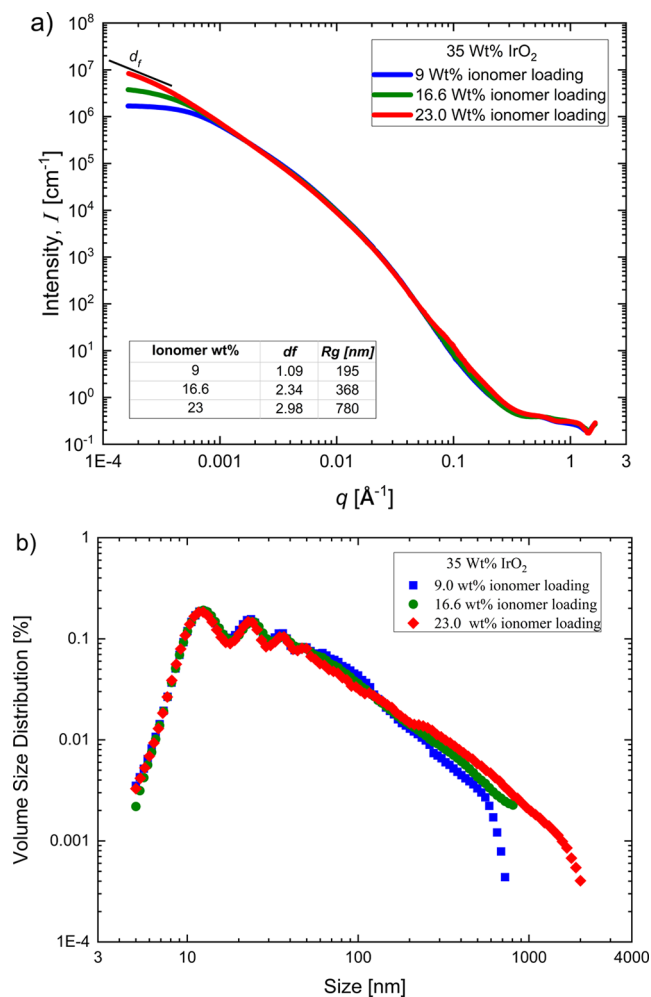


**Figure 11.** (a) USAXS scattering curves. Tabulated values of the mass fractal dimension  $d_f$  from  $I(q) \approx q^{-d_f}$  power-law fit to low- $q$  data and the radius of gyration  $R_g$  at lower- $q$  region from Guinier fit to the data are also shown in pane (a) and (b) volume size distribution of 35 wt % IrO<sub>2</sub> dispersions with different ionomer loadings.

both the  $d_f$  values at low- $q$  (1.09–2.98) and  $R_g$  (195–780 nm) with increasing ionomer loadings from 9 to 23 wt % from Figure 11a. A large increase in the agglomerate populations beyond 200 nm with increasing ionomer loading can also be observed in the volume–size-distribution plot in Figure 11b. These observations confirm the flocculation of the inks at large ionomer loading supporting the rheological observations.

Based on the steady-shear rheological behavior (Figure 8), we previously suggested that beyond 2.4 wt % ionomer



loadings, the ionomer could continue to adsorb onto the particles and/or remain as dispersed polymer in the dispersion medium. Continued adsorption of the ionomer is likely to further stabilize the  $\text{IrO}_2$  particles due to increasing electrosteric repulsion potential. In contrast, an increase in the dispersed ionomer concentration could induce particle flocculation beyond a critical dispersed ionomer concentration. Many studies on colloid–polymer mixtures have found that a nonadsorbing polymer can induce particle flocculation through the depletion flocculation mechanism, where flocculation is driven by osmotic pressure gradients due to differences in the local polymer concentration between the bulk and depletion volume between neighboring particles.<sup>28,58,59</sup> Flocculation by such a mechanism is possible here where the dispersed-ionomer concentration in the inks at large ionomer loadings (16.6 wt % and beyond) could reach a sufficient concentration to induce depletion flocculation.

**Effect of Catalyst Concentration.** Often catalyst ink concentrations are varied to modify the ink rheology to suit a certain coating method for the fabrication of MEA. This is usually done at a fixed optimized ionomer-to-catalyst ratio (or ionomer loading which has been empirically determined for best electrochemical performance). Therefore, the effect of catalyst concentration on the microstructure and rheology of ink formulations was also studied. The  $\text{IrO}_2$  concentrations were varied from 5 to 35 wt % and the ionomer loading was fixed at 16.6 wt % (note that the ionomer concentration w.r.t ink, however, increases with  $\text{IrO}_2$  wt % as the ionomer/catalyst ratio is fixed).

The steady-shear rheology of inks for different  $\text{IrO}_2$  concentrations both with and without the ionomer are compared, as shown in Figure 12a. For lower  $\text{IrO}_2$  concentrations of 5 and 13%, the addition of the ionomer appears to result in an increase in the viscosity. It can be expected that a low number of  $\text{IrO}_2$  agglomerates exists in the ink at low particle concentrations.<sup>58</sup> Thus, the viscosity changes due to any agglomerate stabilization by the ionomer might be small. Rather, the increase in the viscosity is predominantly due to the contribution from the added volume of the ionomer in the inks—adsorbed onto the surface of the particle and/or present in the solvent. This behavior is in agreement with the DLS results on dilute inks where the agglomeration changes due to ionomer stabilization were weak and the  $Z_{\text{avg}}$  predominantly increased with increasing ionomer loading.

In contrast, at higher  $\text{IrO}_2$  concentrations of 25 and 35 wt %, the addition of the ionomer to the inks results in a reduction in both the low-shear viscosities and the magnitude of shear-thinning. This is due to the presence of more agglomerates at higher  $\text{IrO}_2$  concentrations. As a result, the magnitude of agglomerate reduction by the ionomer and the associated effect on viscosity is much more significant compared to the less concentrated inks. However, at lower  $\text{IrO}_2$  concentrations (<35 wt %) with the same ionomer loading, flocculation does not appear prevalent. The steady-shear behavior shown in Figure 12a for  $\text{IrO}_2$  concentrations below 35 wt % is Newtonian and does not exhibit the shear-thinning behavior as observed for 35 wt % ink. The frequency sweep response of the 25 wt %  $\text{IrO}_2$  ink, shown in Figure 12b, is liquid-like ( $G' \approx \omega^1$  and  $G'' \approx \omega^2$ ), and not power-law like the 35 wt %  $\text{IrO}_2$  inks. These observations suggest that flocculation is sensitive to both the  $\text{IrO}_2$  and the ionomer concentration in the inks. As discussed previously, the flocculation in the  $\text{IrO}_2$  inks was

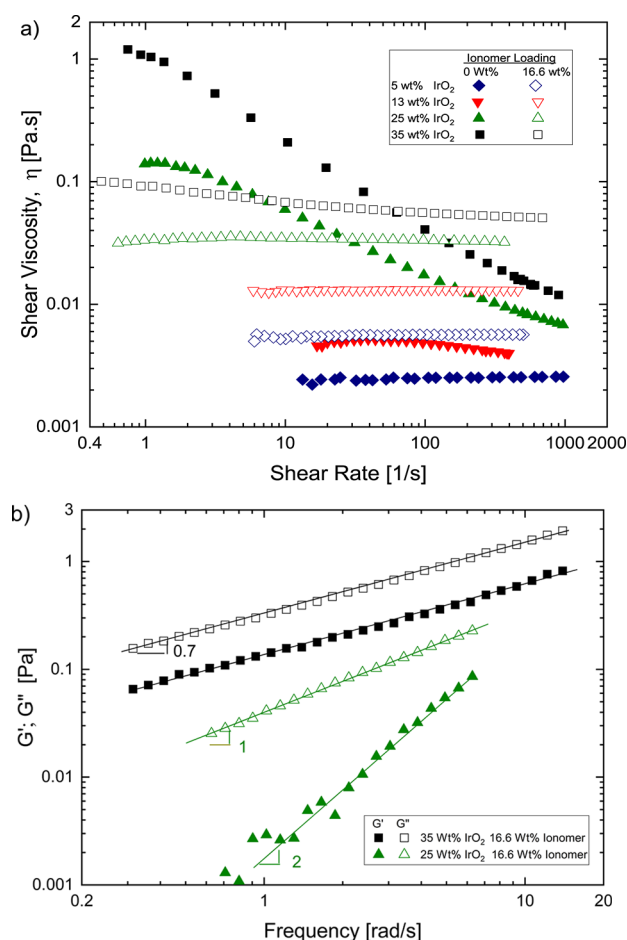


**Figure 12.** (a) Steady-shear rheology data for inks at different  $\text{IrO}_2$  concentrations with fixed 16.6 wt % ionomer loadings. The data for inks with no ionomer is also shown. (b) Frequency-sweep comparison between inks of 35 wt %  $\text{IrO}_2$  and 25 wt %  $\text{IrO}_2$  concentrations at fixed 16.6 wt % ionomer loadings. The lines are only a guide to the eye.

hypothesized to occur through depletion flocculation. The effect of particle and ionomer concentrations on the onset of flocculation behavior observed here is in agreement with previous studies on depletion flocculation.<sup>58,60,61</sup> Depletion is found to occur when the interparticle separation approaches very small distances, less than twice the effective polymer coil size. Increasing the particle volume fraction and/or polymer volume fraction, which reduces the interparticle separation distance, is found to decrease the onset of flocculation.

**Implications for CL Fabrication.** Our observations on the ink structure provide insights for electrode optimization. The results suggest that the addition of the ionomer facilitates dispersion of  $\text{IrO}_2$ . In concentrated inks of 35 wt %  $\text{IrO}_2$ , an ionomer loading as small as 2.4 wt % appears to completely stabilize the agglomerates. Such dispersion of catalyst agglomerates is desired for maximum catalytic utilization. The flocculated ink structure observed at large  $\text{IrO}_2$  concentration (>25 wt %) and large ionomer loadings ( $\geq 16.6$  wt %) could result in a heterogeneous distribution of the ionomer and catalyst in the CL microstructure. This could lead to nonuniform mass transport properties across the CL as well as lower catalyst utilization, which would be undesired for performance. Few studies exist that have examined the influence of ionomer loading on the CL microstructure and

performance.<sup>62–64</sup> However, we are unable to correlate our findings on the ink structure to the performance studies in the literature. The catalyst ink materials used in this study differ from that of the literature in the catalyst type, solvent type, and solvent–H<sub>2</sub>O mixture ratio and thus may influence the ink structure differently and/or to different magnitudes. Thus, more studies are needed to link our observations of the ink microstructure to the CL microstructure and performance.

Additionally, processing during CL fabrication—coating and drying—will also influence the CL microstructure. The ink structure can experience different magnitudes of deformation based on the process type and conditions, which could break-up any agglomerates and/or induce interparticle/ionomer rearrangements. The rheological properties predominantly dictate potential structural changes in the ink during the coating process.<sup>16,53</sup> Furthermore, the drying process could also significantly impact both the particle and ionomer distribution in the CL, where the rheological properties have also been shown to play a significant role in the evolution of the colloidal film structure during drying.<sup>65</sup> Given the differences in the rheological behavior as a function of the catalyst and ionomer loadings in these inks, we may expect the coating and drying processes to affect the evolution of the CL microstructure differently. However, the effects of processing on the CL microstructure are still poorly understood. We believe the observations of the ink structure and rheological behavior from this study will enable further studies in understanding the relationships between the ink structure and CL processing and the resulting CL microstructure and performance.

## CONCLUSIONS

We have presented an investigation of the microstructure of catalyst inks consisting of the IrO<sub>2</sub> catalyst and ionomer dispersed in a 1-propanol–water solvent mixture. The effects of ionomer loadings and IrO<sub>2</sub> concentration were investigated using rheology in combination with other techniques such as DLS,  $\zeta$ -potential, and USAXS. The main conclusions from the study are (i) the IrO<sub>2</sub> particles are agglomerated in the absence of ionomer in the ink, where the degree of agglomeration increases with the particle concentration; (ii) the ionomer strongly interacts with the catalyst particles by adsorbing onto particle surface and disperses any agglomerated structure in the ink; (iii) at 2.4 wt % ionomer loading, the agglomerates achieved a maximum stability in concentrated inks (35 wt % IrO<sub>2</sub>); and (iv) at large ionomer loadings ( $\geq 16.6$  wt %) in concentrated dispersions ( $> 25$  wt % IrO<sub>2</sub>), the dispersed ionomer is found to induce flocculation of the particles likely through depletion flocculation. The insights gained from this study on the catalyst–ionomer interactions are valuable toward optimizing catalyst ink formulations. From the perspective of processing, the differences in the rheological behaviors such as Newtonian or shear-thinning, depending on the IrO<sub>2</sub> concentration and ionomer loading in the formulation, could influence the coating and drying processes differently and affect the formation of the CL microstructure.

## AUTHOR INFORMATION

### Corresponding Author

\*E-mail: [scott.mauger@nrel.gov](mailto:scott.mauger@nrel.gov).

### ORCID

Sunilkumar Khandavalli: 0000-0003-3179-5718

Svitlana Pylypenko: 0000-0001-7982-734X

Scott A. Mauger: 0000-0003-2787-5029

## Notes

The authors declare no competing financial interest.

## ACKNOWLEDGMENTS

The authors would like to thank Jan Ilavsky and Ivan Kuzmenko of APS 9-ID for assistance with USAXS measurements and Katherine Hurst of NREL for N<sub>2</sub> adsorption measurements. This work was authored in part by Alliance for Sustainable Energy, LLC, the manager and operator of the National Renewable Energy Laboratory for the U.S. Department of Energy (DOE) under contract no. DE-AC36-08GO28308. Funding was provided by U.S. Department of Energy Office of Energy Efficiency and Renewable Energy Fuel Cell Technologies Office, Program Manager Nancy Garland. The submitted manuscript was created, in part, by UChicago Argonne, LLC, Operator of Argonne National Laboratory, Argonne, U.S. Department of Energy Office of Science laboratory, operated under contract no. DE-AC02-06CH11357. This research used the resources of the Advanced Photon Source (APS), a U.S. Department of Energy (DOE) Office of Science User Facility, operated for the DOE Office of Science by Argonne National Laboratory, also under contract no. DE-AC02-06CH11357. The views expressed in the article do not necessarily represent the views of the DOE or the U.S. Government. The U.S. Government retains and the publisher, by accepting the article for publication, acknowledges that the U.S. Government retains a nonexclusive, paid-up, irrevocable, worldwide license to publish or reproduce the published form of this work, or allow others to do so, for U.S. Government purposes.

## REFERENCES

- (1) Grigoriev, S.; Porembsky, V.; Fateev, V. Pure Hydrogen Production by PEM Electrolysis for Hydrogen Energy. *Int. J. Hydrogen Energy* **2006**, *31*, 171–175.
- (2) Carmo, M.; Fritz, D. L.; Mergel, J.; Stolten, D. A Comprehensive Review on PEM Water Electrolysis. *Int. J. Hydrogen Energy* **2013**, *38*, 4901–4934.
- (3) Barbir, F. PEM Electrolysis for Production of Hydrogen from Renewable Energy Sources. *Sol. Energy* **2005**, *78*, 661–669.
- (4) Holdcroft, S. Fuel Cell Catalyst Layers: A Polymer Science Perspective. *Chem. Mater.* **2014**, *26*, 381–393.
- (5) Hatzell, K. B.; Dixit, M. B.; Berlinger, S. A.; Weber, A. Z. Understanding Inks for Porous-Electrode Formation. *J. Mater. Chem. A* **2017**, *5*, 20527–20533.
- (6) Mauger, S. A.; Neyerlin, K. C.; Yang-Neyerlin, A. C.; More, K. L.; Ulsh, M. Gravure Coating for Roll-to-Roll Manufacturing of Proton-Exchange-Membrane Fuel Cell Catalyst Layers. *J. Electrochem. Soc.* **2018**, *165*, F1012–F1018.
- (7) Litster, S.; McLean, G. PEM Fuel Cell Electrodes. *J. Power Sources* **2004**, *130*, 61–76.
- (8) Ma, L.; Sui, S.; Zhai, Y. Investigations on High Performance Proton Exchange Membrane Water Electrolyzer. *Int. J. Hydrogen Energy* **2009**, *34*, 678–684.
- (9) Xu, W.; Scott, K. The Effects of Ionomer Content on PEM Water Electrolyser Membrane Electrode Assembly Performance. *Int. J. Hydrogen Energy* **2010**, *35*, 12029–12037.
- (10) Berni, M.; Gasteiger, H. A. Influence of Ionomer Content in IrO<sub>2</sub>/TiO<sub>2</sub> Electrodes on PEM Water Electrolyzer Performance. *J. Electrochem. Soc.* **2016**, *163*, F3179–F3189.
- (11) Khandavalli, S.; Park, J. H.; Kariuki, N. N.; Myers, D. J.; Stickel, J. J.; Hurst, K.; Neyerlin, K. C.; Ulsh, M.; Mauger, S. A. Rheological

Investigation on the Microstructure of Fuel Cell Catalyst Inks. *ACS Appl. Mater. Interfaces* **2018**, *10*, 43610–43622.

(12) Hoogeveen, N. G.; Stuart, M. A. C.; Fleer, G. J. Can Charged (Block Co)Polymers Act as Stabilisers and Flocculants of Oxides? *Colloids Surf., A* **1996**, *117*, 77–88.

(13) Morelly, S. L.; Alvarez, N. J.; Tang, M. H. Short-Range Contacts Govern the Performance of Industry-Relevant Battery Cathodes. *J. Power Sources* **2018**, *387*, 49–56.

(14) Kistler, S. F.; Schweizer, P. M. In *Liquid Film Coating*; Kistler, S. F., Schweizer, P. M., Eds.; Springer Netherlands: Dordrecht, 1997; pp 137–180.

(15) Khandavalli, S.; Lee, J. A.; Pasquali, M.; Rothstein, J. P. The Effect of Shear-Thickening on Liquid Transfer from an Idealized Gravure Cell. *J. Non-Newtonian Fluid Mech.* **2015**, *221*, 55–65.

(16) Khandavalli, S.; Rothstein, J. P. The Effect of Shear-Thickening on the Stability of Slot-Die Coating. *AIChE J.* **2016**, *62*, 4536–4547.

(17) Dixit, M. B.; Harkey, B. A.; Shen, F.; Hatzell, K. B. Catalyst Layer Ink Interactions That Affect Coatability. *J. Electrochem. Soc.* **2018**, *165*, F264–F271.

(18) Ding, X.; Harris, T. A. L. Review on Penetration and Transport Phenomena in Porous Media During Slot Die Coating. *J. Polym. Sci. B* **2017**, *55*, 1669–1680.

(19) Moore, M.; Wardlaw, P.; Dobson, P.; Boisvert, J. J.; Putz, A.; Spiteri, R. J.; Secanell, M. Understanding the Effect of Kinetic and Mass Transport Processes in Cathode Agglomerates. *J. Electrochem. Soc.* **2014**, *161*, E3125–E3137.

(20) Dixit, M. B.; Harkey, B. A.; Shen, F.; Hatzell, K. B. Catalyst Layer Ink Interactions That Affect Coatability. *J. Electrochem. Soc.* **2018**, *165*, F264–F271.

(21) Kaszuba, M.; Corbett, J.; Watson, F. M.; Jones, A. High-Concentration Zeta Potential Measurements Using Light-Scattering Techniques. *Philos. Trans. R. Soc., A* **2010**, *368*, 4439–4451.

(22) Hunter, R. J. Chapter 3: The Calculation of Zeta Potential. In *Zeta Potential in Colloid Science*; Hunter, R. J., Ed.; Academic Press, 1981; pp 59–124.

(23) Zhang, H.; Pan, J.; He, X.; Pan, M. Zeta Potential of Nafion Molecules in Isopropanol-Water Mixture Solvent. *J. Appl. Polym. Sci.* **2008**, *107*, 3306–3309.

(24) Berlinger, S. A.; McCloskey, B. D.; Weber, A. Z. Inherent Acidity of Perfluorosulfonic Acid Ionomer Dispersions and Implications for Ink Aggregation. *J. Phys. Chem. B* **2018**, *122*, 7790–7796.

(25) Li, G.-F.; Yang, D.; Abel Chuang, P.-Y. Defining Nafion Ionomer Roles for Enhancing Alkaline Oxygen Evolution Electrocatalysis. *ACS Catal.* **2018**, *8*, 11688–11698.

(26) Barany, S. Polymer Adsorption and Electrokinetic Potential of Dispersed Particles in Weak and Strong Electric Fields. *Adv. Colloid Interface Sci.* **2015**, *222*, 58–69.

(27) Abbott, D. F.; Lebedev, D.; Waltar, K.; Povia, M.; Nachtegaal, M.; Fabbri, E.; Copéret, C.; Schmidt, T. J. Iridium Oxide for the Oxygen Evolution Reaction: Correlation between Particle Size, Morphology, and the Surface Hydroxyl Layer from Operando XAS. *Chem. Mater.* **2016**, *28*, 6591–6604.

(28) Mewis, J.; Wagner, N. J. *Colloidal Suspension Rheology*; Cambridge University Press: Cambridge, 2011; pp 157–179.

(29) Israelachvili, J. N. *Intermolecular and Surface Forces*; Israelachvili, J. N., Ed.; Academic Press: Cambridge, 2011; pp 238–239.

(30) Méndez-Bermúdez, J. G.; Dominguez, H.; Pusztai, L.; Guba, S.; Horváth, B.; Szalai, I. Composition and Temperature Dependence of the Dielectric Constant of 1-Propanol/Water Mixtures: Experiment and Molecular Dynamics Simulations. *J. Mol. Liq.* **2016**, *219*, 354–358.

(31) Yamaguchi, M.; Matsunaga, T.; Amemiya, K.; Ohira, A.; Hasegawa, N.; Shinohara, K.; Ando, M.; Yoshida, T. Dispersion of Rod-like Particles of Nafion in Salt-Free Water/1-Propanol and Water/Ethanol Solutions. *J. Phys. Chem. B* **2014**, *118*, 14922–14928.

(32) Takahashi, S.; Shimanuki, J.; Mashio, T.; Ohma, A.; Tohma, H.; Ishihara, A.; Ito, Y.; Nishino, Y.; Miyazawa, A. Observation of

Ionomer in Catalyst Ink of Polymer Electrolyte Fuel Cell Using Cryogenic Transmission Electron Microscopy. *Electrochim. Acta* **2017**, *224*, 178–185.

(33) Shukla, S.; Bhattacharjee, S.; Weber, A. Z.; Secanell, M. Experimental and Theoretical Analysis of Ink Dispersion Stability for Polymer Electrolyte Fuel Cell Applications. *J. Electrochem. Soc.* **2017**, *164*, F600–F609.

(34) Larson, R. G. *The Structure and Rheology of Complex Fluids*; Larson, R. G., Ed.; Oxford University Press Inc.: New York, 1999; pp 263–355.

(35) Fritz, G.; Schädler, V.; Willenbacher, N.; Wagner, N. J. Electrosteric Stabilization of Colloidal Dispersions. *Langmuir* **2002**, *18*, 6381–6390.

(36) Derjaguin, B.; Landau, L. Theory of the Stability of Lyophobic Colloids: The Interaction of Sol Particles Having an Electric Double Layer. *Acta Physicochim. URSS* **1941**, *14*, 633–662.

(37) Verwey, E. J. W.; Overbeek, J. T. G. *Theory of the Stability of Lyophobic Colloids: The Interaction of Sol Particles Having an Electric Double Layer*; Elsevier, Amsterdam, 1948; pp 135–662.

(38) Wang, M.; Park, J. H.; Kabir, S.; Neyerlin, K. C.; Kariuki, N. N.; Lv, H.; Stamenkovic, V. R.; Myers, D. J.; Ulsh, M.; Mauger, S. A. Impact of Catalyst Ink Dispersing Methodology on Fuel Cell Performance Using in-Situ X-ray Scattering. *ACS Appl. Energy Mater.* **2019**, *2*, 6417–6427.

(39) Hunter, R. J. The Calculation of Zeta Potential. *Zeta Potential in Colloid Science*; Academic Press, 1981; pp 59–124.

(40) Alia, S. M.; Anderson, G. C. Iridium Oxygen Evolution Activity and Durability Baselines in Rotating Disk Electrode Half-Cells. *J. Electrochem. Soc.* **2019**, *166*, F282–F294.

(41) Babic, U.; Nilsson, E.; Pătru, A.; Schmidt, T. J.; Gubler, L. Proton Transport in Catalyst Layers of a Polymer Electrolyte Water Electrolyzer: Effect of the Anode Catalyst Loading. *J. Electrochem. Soc.* **2019**, *166*, F214–F220.

(42) Wagner, N. J.; Brady, J. F. Shear Thickening in Colloidal Dispersions. *Phys. Today* **2009**, *62*, 27–32.

(43) Khandavalli, S.; Rothstein, J. P. Extensional Rheology of Shear-Thickening Fumed Silica Nanoparticles Dispersed in an Aqueous Polyethylene Oxide Solution. *J. Rheol.* **2014**, *58*, 411–431.

(44) Batchelor, G. K. The Effect of Brownian Motion on the Bulk Stress in a Suspension of Spherical Particles. *J. Fluid Mech.* **1977**, *83*, 97–117.

(45) Bergenholtz, J.; Brady, J. F.; Vivic, M. The Non-Newtonian Rheology of Dilute Colloidal Suspensions. *J. Fluid Mech.* **2002**, *456*, 239–275.

(46) Krieger, I. M.; Dougherty, T. J. A Mechanism for Non-Newtonian Flow in Suspensions of Rigid Spheres. *Trans. Soc. Rheol.* **1959**, *3*, 137–152.

(47) Smith, T. L.; Bruce, C. A. Intrinsic Viscosities and Other Rheological Properties of Flocculated Suspensions of Nonmagnetic and Magnetic Ferric Oxides. *J. Colloid Interface Sci.* **1979**, *72*, 13–26.

(48) Rubio-Hernández, F. J.; Ayúcar-Rubio, M. F.; Velázquez-Navarro, J. F.; Galindo-Rosales, F. J. Intrinsic Viscosity of SiO<sub>2</sub>, Al<sub>2</sub>O<sub>3</sub> and TiO<sub>2</sub> Aqueous Suspensions. *J. Colloid Interface Sci.* **2006**, *298*, 967–972.

(49) de Kruij, C. G.; van Iersel, E. M. F.; Vrij, A.; Russel, W. B. Hard Sphere Colloidal Dispersions: Viscosity as a Function of Shear Rate and Volume Fraction. *J. Chem. Phys.* **1985**, *83*, 4717–4725.

(50) Mizukawa, H.; Kawaguchi, M. Effects of Perfluorosulfonic Acid Adsorption on the Stability of Carbon Black Suspensions. *Langmuir* **2009**, *25*, 11984–11987.

(51) Beaucage, G. Small-Angle Scattering from Polymeric Mass Fractals of Arbitrary Mass-Fractal Dimension. *J. Appl. Crystallogr.* **1996**, *29*, 134–146.

(52) Andrews, R. N.; Serio, J.; Muralidharan, G.; Ilavsky, J. An in situ SAXS-SAXS-WAXS study of precipitate size distribution evolution in a model Ni-based alloy. *J. Appl. Crystallogr.* **2017**, *50*, 734–740.

(53) Khandavalli, S.; Rothstein, J. P. Ink Transfer of Non-Newtonian Fluids from an Idealized Gravure Cell: The Effect of Shear and



Extensional Deformation. *J. Non-Newtonian Fluid Mech.* **2017**, *243*, 16–26.

(54) Laurati, M.; Petekidis, G.; Koumakis, N.; Cardinaux, F.; Schofield, A. B.; Brader, J. M.; Fuchs, M.; Egelhaaf, S. U. Structure, Dynamics, and Rheology of Colloid-Polymer Mixtures: From Liquids to Gels. *J. Chem. Phys.* **2009**, *130*, 134907.

(55) Winter, H. H.; Chambon, F. Analysis of Linear Viscoelasticity of a Crosslinking Polymer at the Gel Point. *J. Rheol.* **1986**, *30*, 367–382.

(56) Aoki, Y.; Hatano, A.; Watanabe, H. Rheology of Carbon Black Suspensions. I. Three Types of Viscoelastic Behavior. *Rheol. Acta* **2003**, *42*, 209–216.

(57) Khandavalli, S.; Rothstein, J. P. Large Amplitude Oscillatory Shear Rheology of Three Different Shear-Thickening Particle Dispersions. *Rheol. Acta* **2015**, *54*, 601–618.

(58) Pagac, E. S.; Tilton, R. D.; Prieve, D. C. Depletion Attraction Caused by Unadsorbed Polyelectrolytes. *Langmuir* **1998**, *14*, 5106–5112.

(59) Szilagyi, I.; Trefalt, G.; Tiraferri, A.; Maroni, P.; Borkovec, M. Polyelectrolyte Adsorption, Interparticle Forces, and Colloidal Aggregation. *Soft Matter* **2014**, *10*, 2479–2502.

(60) Liang, W.; Tadros, T. F.; Luckham, P. F. Flocculation of Sterically Stabilized Polystyrene Latex Particles by Adsorbing and Nonadsorbing Poly(Acrylic Acid). *Langmuir* **1994**, *10*, 441–446.

(61) Ogden, A. L.; Lewis, J. A. Effect of Nonadsorbed Polymer on the Stability of Weakly Flocculated Suspensions. *Langmuir* **2002**, *12*, 3413–3424.

(62) Mandal, M.; Valls, A.; Gangnus, N.; Secanell, M. Analysis of Inkjet Printed Catalyst Coated Membranes for Polymer Electrolyte Electrolyzers. *J. Electrochem. Soc.* **2018**, *165*, F543–F552.

(63) Marshall, A.; Sunde, S.; Tsyppkin, M.; Tunold, R. Performance of a PEM water electrolysis cell using IrxRu<sub>y</sub>TazO<sub>2</sub>IrxRu<sub>y</sub>TazO<sub>2</sub> electrocatalysts for the oxygen evolution electrode. *Int. J. Hydrogen Energy* **2007**, *32*, 2320–2324.

(64) Rasten, E.; Hagen, G.; Tunold, R. Electrocatalysis in Water Electrolysis with Solid Polymer Electrolyte. *Electrochim. Acta* **2003**, *48*, 3945–3952.

(65) Haw, M. D.; Gillie, M.; Poon, W. C. K. Effects of Phase Behavior on the Drying of Colloidal Suspensions. *Langmuir* **2002**, *18*, 1626–1633.